

# Grain Boundary Sliding During High Pressure Torsion of Nanocrystalline Au-13Pd Alloy

Werner Skrotzki,\* Aurimas Pukenas, Bertalan Jóni, Tamas Ungár, Laszlo S. Toth, and Yulia Ivanisenko

Dedicated to Prof. Dr. Reinhard Pippan on the occasion of his 70th birthday.

The microstructure and texture are investigated for nanocrystalline Au-13at%Pd deformed by high-pressure torsion. The grain size of this alloy is observed to remain below about 20 nm when subjected to severe plastic deformation. Surprisingly, the initial  $\langle 110 \rangle$  powder compaction texture does not change significantly during shearing. The results are explained in terms of a grain boundary sliding mechanism involving planar interfaces formed by grain boundary migration.

## 1. Introduction

For polycrystalline materials with decreasing grain size, the mechanical properties are increasingly determined by their grain boundaries. This plasticity mediated by grain boundaries dominates at grain sizes in the lower nanosize range<sup>[1–8]</sup> and leads to “grain size softening,” also called “inverse Hall–Petch behavior.”<sup>[9,10]</sup> In addition, texture formation is significantly reduced.<sup>[1–8]</sup> These characteristic features indicate a kind of superplastic behavior dominated by grain boundary-mediated deformation. How this deformation process actually occurs is still unclear. For nanocrystalline (nc) materials, the deformation mediated by grain boundaries is considered as a cooperative shear process involving multiple grains.<sup>[11]</sup> Another approach is to assign the grain boundaries to an amorphous structure in which shear shuffling or shear transformation takes place.<sup>[12]</sup> Since the atomistic nature of the grain boundary shearing process is not modeled in the present work, this process is hereinafter referred to simply as grain boundary sliding (GBS) using general terminology. It should also be noted that in addition to GBS, grain boundary migration also occurs, leading to grain growth due to stress-induced shear coupling.<sup>[3,13]</sup>

In the present work, the microstructure and texture evolution are studied on a nc Au-13at%Pd alloy (hereinafter referred to as Au-13Pd) fabricated and deformed by high-pressure torsion (HPT) in the same way as the nc Pd-10Au alloy.<sup>[3]</sup> The main differences between Au-13Pd to the former alloy are the lower melting temperature, respectively, higher homologous deformation temperature (1473 K, 0.20, compared to 1813 K, 0.16<sup>[14]</sup> (factor 1.25)) and significantly lower stacking fault energy (SFE) (40 mJ m<sup>−2</sup> compared to 150 mJ m<sup>−2</sup><sup>[15]</sup> (factor 3.75)). Both effects affect the operation of GBS and mechanical twinning. Recently, a new GBS model was developed by Zhao et al.<sup>[4]</sup> and successfully applied to the texture evolution of the nc Pd-10Au alloy.<sup>[5]</sup> That model is applied here on the HPT-deformed nc Au-13Pd alloy. By comparing experimental and simulated texture results, conclusions are drawn about the mechanism of GBS as the dominant deformation mechanism.

## 2. Experimental and Modeling

Nanocrystalline Au-13Pd powder was produced by inert gas condensation (igc)<sup>[16]</sup> using a 10<sup>−7</sup> mbar base pressure vacuum

W. Skrotzki, A. Pukenas  
Institut für Festkörper-und Materialphysik  
Technische Universität Dresden  
D-01062 Dresden, Germany  
E-mail: werner.skrotzki@tu-dresden.de


B. Jóni, T. Ungár  
Department of Materials Physics  
Budapest Eötvös University  
H-1117 Budapest, Hungary

L. S. Toth  
Institute of Physical Metallurgy, Metal-forming and Nanotechnology  
University of Miskolc  
3515 Miskolc, Hungary

L. S. Toth  
Laboratoire d'Étude des Microstructures et de Mécanique des Matériaux (LEM3)  
Université de Lorraine – Metz  
F-57045 Metz Cedex 01, France

L. S. Toth  
Laboratory of Excellence on Design of Alloy Metals for low-mAss Structures (DAMAS)  
Université de Lorraine  
F-57045 Metz, France

Y. Ivanisenko  
Institut für Nanotechnologie  
Karlsruher Institut für Technologie (KIT)  
D-76021 Karlsruhe, Germany

 The ORCID identification number(s) for the author(s) of this article can be found under <https://doi.org/10.1002/adem.202400214>.

© 2024 The Author(s). Advanced Engineering Materials published by Wiley-VCH GmbH. This is an open access article under the terms of the Creative Commons Attribution License, which permits use, distribution and reproduction in any medium, provided the original work is properly cited.

DOI: 10.1002/adem.202400214

system and thermal evaporation of Au (99.95%) and Pd (99.95%) in a 1 mbar helium atmosphere. The powder was consolidated in situ at a pressure of 2 GPa to obtain disc-shaped specimens with a diameter of 8 mm and thickness of about 0.7 mm (first compaction step). Chemical analysis was done by energy-dispersive X-ray spectroscopy. The nc samples exhibit a stable grain size even at temperatures well above ambient, in contrast to pure nc materials where rapid grain coarsening is observed at room temperature.<sup>[17]</sup>

Quasi-hydrostatic HPT<sup>[18]</sup> was conducted under a pressure of 6 GPa in a custom-made computer-controlled HPT machine manufactured by W. Klement GmbH (Lang, Austria). The sample was twisted up to a rotation angle  $\theta = 200^\circ$  at a constant rate of  $6^\circ \text{ s}^{-1}$  (1 rpm). During HPT, the shear strain along the radius  $r$  is approximately given by:

$$\gamma = 2\pi r \theta / (360^\circ t) \quad (1)$$

where  $t$  is the initial disc thickness. With  $t = 0.713 \text{ mm}$ , the maximum shear strain and shear strain rate were 19.7 and  $0.6 \text{ s}^{-1}$ , respectively. The reduction of thickness by 4% during HPT has been neglected. The torque was measured by means of a full bridge torsion-shear and tension-compression strain gauge (Hottinger Baldwin Messtechnik GmbH, Darmstadt, Type 1-XY41-3/350 and XY71-3/350). The HPT friction-corrected torque  $T$  was transformed into shear stress  $\tau$  using the Nadai formula,<sup>[19]</sup> established for torsion

$$\tau = \frac{T}{2\pi a^3} \left( 3 + \frac{d \ln T}{d \ln \theta} \right) \quad (2)$$

where  $\tau$  is valid for the outer radius  $r = a$ . In this calculation, the measured torque values were lowered with the torque generated by the friction between the sample's outer cylinder surface and the die ( $T_f$ ). This part of the torque is generated by the friction force due to the hydrostatic pressure  $p$  within the sample which is pushing the lateral surface of the sample to the die. It is not contributing to the shear stress  $\tau$ . In HPT testing, it is widely accepted that the hydrostatic pressure is equal to the compression pressure  $p$ . Thus, using Coulomb's friction law,  $T_f$  can be calculated by

$$T_f = 2\pi \mu p t a^2 \quad (3)$$

Using this approach, the friction torques have been estimated by taking a friction coefficient of  $\mu = 0.15$ . This value of the friction coefficient was inspired by the special friction experiments of ref. [20] carried out for large pressures.

The density determined by the Archimedes method during HPT changed from about 91% after the first compaction step to about 97% of that of the bulk in the second compaction step.<sup>[21,22]</sup> This is about the theoretical density of a bulk nc material taking into account the free volume in the grain boundaries.<sup>[22]</sup>

To investigate the microstructure, X-ray diffraction measurements were carried out in a special high-resolution diffractometer dedicated to X-ray line profile analysis (XLPA)<sup>[23]</sup> using Cu  $K_\alpha$  radiation, for details see refs. [24,25]. The measurements are done along the radius of the HPT discs, i.e., at positions where the shear strains are different. The line profiles are evaluated by

using the convolutional multiple whole profile (CMWP) procedure.<sup>[26]</sup> The measured diffraction pattern is matched by the theoretically calculated and convoluted profile functions accounting for the effects of size, distortion, planar defects, and instrumental effects, while the background is determined separately. Because of the double-crystal high-resolution diffractometer used, the instrumental effect is neglected. The parameters obtained by using the CMWP method characterizing the substructure are the area average crystallite (subgrain) size  $\langle x \rangle_a$ , dislocation density  $\rho$ , dislocation character  $q$  (edge versus screw), dislocation arrangement parameter  $M = R_e \sqrt{\rho}$  ( $R_e$  = effective outer cut-off radius of dislocations), and twin density  $\beta$  (number of twin boundary planes for each hundred {111} lattice planes parallel to the twin boundaries).<sup>[27]</sup>

To resolve the local texture of the deformed discs along the radial direction from the center to the edge of the disc, i.e., as a function of increasing shear strain, two-dimensional X-ray microdiffraction was applied using the system D8 Discover (BRUKER AXS GmbH) equipped with an Euler cradle including x-y-z-stage, a laser-video adjustment system, a low-power micro-focus X-ray tube  $\text{I}\mu\text{S}$  (spot size about 100  $\mu\text{m}$ ) and a two-dimensional detector VANTEC 2000. Before testing, the samples were mechanically polished and finally chemically etched to remove any surface layer damaged by the deformation procedure. The intensities of the measured Debye-Scherrer rings were integrated along their curvature to calculate the pole figures (PFs) (200, 220, 111) on a  $5^\circ \times 5^\circ$  grid. For calculation of the orientation distribution function (ODF) with these PFs, Maltex 3<sup>[28]</sup> and LaboTex software<sup>[29]</sup> were used. The Euler angles given are in the Bunge notation<sup>[30]</sup> with crystal and sample reference systems defined as  $x \parallel$  shear direction (SD),  $y \parallel$  shear plane normal (SPN), and  $z \parallel$  transverse direction (TD) yielding an ODF representation appropriate for simple shear.<sup>[31]</sup> The textures are represented by  $\varphi_2 = 0^\circ$  and  $\varphi_2 = 45^\circ$  ODF-sections, which for face-centered cubic (fcc) metals contain all major shear components.<sup>[31]</sup>

The modeling of the texture evolution during the compression stages (compaction of igc powder and application of HPT pressure) and HPT shearing was tempted using the GBS approach presented in an earlier work,<sup>[4]</sup> which is a mean field type model. A critical point in modeling the behavior of powder metal is to apply boundary conditions that approximate best the experimental behavior. It is plausible that the compaction of the initial powder involves nearly free rotations and sliding of the particles as well as deformation components that are totally relaxed. Keeping this in mind, only one boundary condition was imposed during the compression, namely, the compression direction applied to the powder was kept constant.

For an ideal case of a powder, when the particles have equal sizes and are spherical, they can be arranged into a close-packed structure with the relative nonfilled volume, i.e., the initial porosity  $f_0$  equal to 0.26. Assuming that the porosity is totally eliminated by the compression leads to a compression strain of  $-0.3$ . In the real powder material, the geometry is not ideal, and there remains some porosity  $f$  as well. Including the free volume in the grain boundaries,<sup>[21,22]</sup> the remaining total porosity can be assumed to be approximately  $f = 0.03$ . With the initial and final porosities, the incompressibility condition of the metal leads to a compression strain of  $\epsilon = -0.27$ .<sup>[32]</sup>

For the powder compaction, the texture simulations were done in small compression strain increments of  $\Delta\epsilon = -0.01$ . The powder was composed of 50 000 initially randomly oriented single crystalline particles with equal volume fractions. The GBS model presented in ref. [4] was applied by employing the relaxed velocity gradient tensor together with the corresponding stress tensor in mixed boundary conditions. Only slip by full dislocations from the grain boundaries in nc materials cannot be significantly active because no grain boundaries are initially present and the grain boundaries form gradually during compression. Details on the simulations of texture formation during the compaction of nanoscale powder can be found in ref. [32].

For the HPT texture simulation, the GBS model of ref. [4] was employed, starting with 10 000 orientations of the experimental initial compaction texture and using shear strain increments of  $\Delta\gamma = 0.05$ . The  $\{111\}\langle 110 \rangle$  and  $\{111\}\langle 112 \rangle$  fcc slip systems were used together with the 12 GBS shear systems without strain hardening. The ratios of the slip system strengths were 1.0/1.5/0.19 for  $\{111\}\langle 112 \rangle/\{111\}\langle 110 \rangle$ /GBS, respectively, with strain rate sensitivity index of 0.125 for  $\{111\}\langle 110 \rangle$  and  $\{111\}\langle 112 \rangle$  slips and 1.0 for GBS. Based on the experience from ref. [8] mechanical twinning was neglected. In all texture simulations, the ODFs were calculated using ATEx software.<sup>[33]</sup>

### 3. Results

The torque–twist angle curve of Au-13Pd in comparison with Pd-10Au is shown in **Figure 1a** together with the curves corrected for friction at the side walls of the HPT pistons. Au-13Pd work hardens less than Pd-10Au and has a lower shear stress (Figure 1b). The waviness of the shear stress–shear strain curve of Au-13Pd in Figure 1a is an artifact of fitting the corrected torque–twist angle curve of Figure 1a. Note that the initial parts of these curves are certainly influenced by the compaction process and therefore may not be precise for the shear stress values.

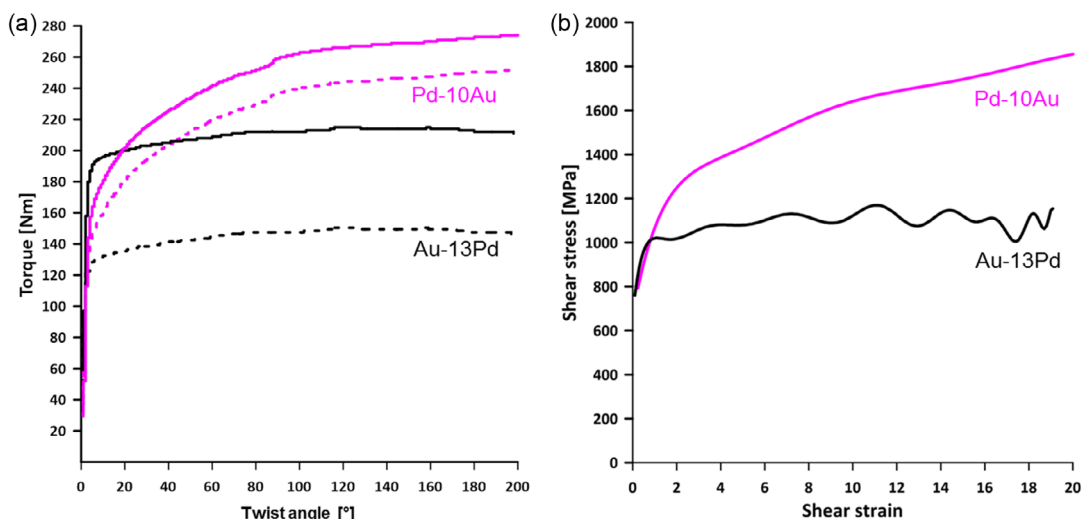


**Figure 1.** a) Experimental HPT torque–twist angle curves of nc Au-13Pd and Pd-10Au alloys together with curves (dashed) corrected for friction at the side walls (friction torques: Au-13Pd: 22.6 Nm, Pd-10Au: 64.5 Nm), where the data are fitted with 10th order polynomial functions. b) Shear stress–shear strain curves derived from the corrected curves of (a).

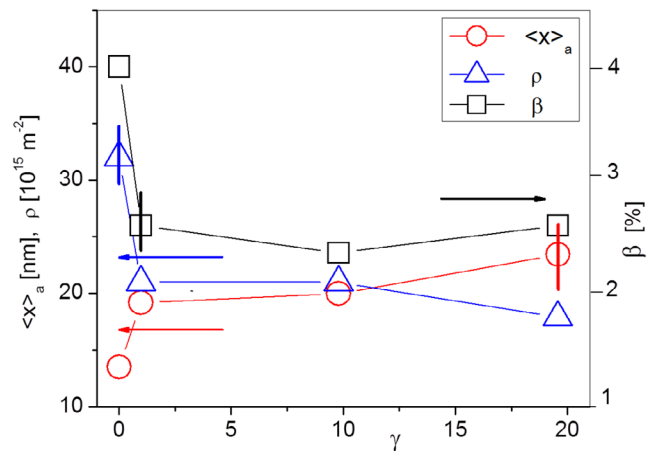


**Figure 2.** Area average mean crystallite size  $\langle x \rangle_a$ , dislocation density  $\rho$ , and twin density  $\beta$  as a function of shear strain  $\gamma$  of HPT-deformed Au-13Pd alloy.

The microstructure parameters determined by XLPa are shown in **Figure 2** and **3** and listed in **Table 1** as a function of shear strain. There is a rapid increase of the area average mean crystallite size  $\langle x \rangle_a$  from 13.5 nm to about a saturation value of about 20 nm at a shear strain of one. In contrast, the dislocation density  $\rho$  and twin density  $\beta$  up to the same shear strain rapidly decrease to minimum values of about  $2 \times 10^{16} \text{ m}^{-2}$  and 2.5, respectively. The measured  $q$  parameter values indicate that the dislocation character is more screw than edge type. The low  $M$  parameter values show that the dislocations are arranged into dipoles or low-angle grain boundaries.

The first compaction stage took place in the powder consolidation unit under 2 GPa pressure which led to the texture shown in **Figure 4**, called “initial.” This texture is extremely weak with a maximum intensity in the ODF of only about 1.5. Then the sample was further compacted in the HPT equipment up to a

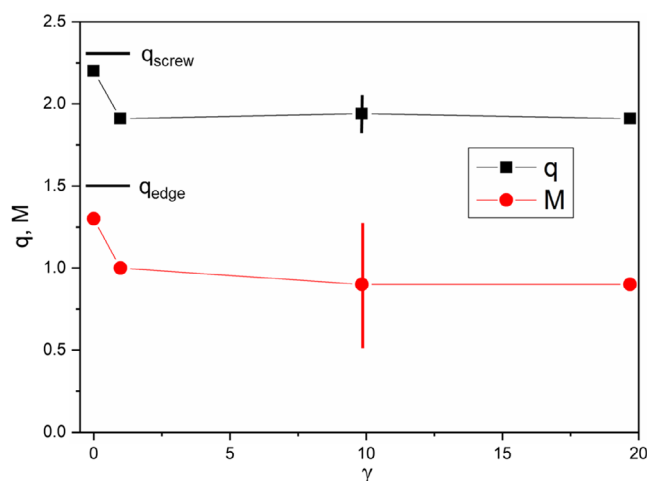


**Figure 3.** Dislocation character  $q$  and dislocation arrangement parameter  $M$  versus shear strain  $\gamma$  of HPT-deformed Au-13Pd alloy ( $q = 1.5$  means pure edge- and  $q = 2.3$  pure screw-type dislocation).

**Table 1.** The results of the CMWP fitting for Au-13Pd at different shear strains  $\gamma$ :  $m$ , median;  $\sigma_{LN}$ , logarithmic variance of the log-normal size distribution;  $\langle X \rangle_{area}$ , average crystallite size;  $\rho$ , dislocation density;  $\beta$ , density of twin boundaries;  $q$ , dislocation character;  $M$ , dislocation arrangement parameter.

$\gamma$	$m$ [nm]	$\sigma_{LN}$	$\langle X \rangle_a$ [nm]	$\rho$ [ $10^{16} \text{ m}^{-2}$ ]	$\beta$ [%]	$q$	$M$
0	8.7	0.42	13.5	3.2	4.0	2.2	1.3
1.0	9.5	0.53	19.2	2.1	2.6	1.91	1.0
9.8	9.9	0.53	20.0	2.1	2.4	1.94	0.9
19.7	13.8	0.46	23.4	1.8	2.6	1.91	0.9

compression stress of 6 GPa and probably slightly more during torsion. During this second compaction, the texture intensity in the center of the sample increased up to 2, its state is identified as  $\gamma = 0$  in Figure 4. This texture is composed of a  $\langle 110 \rangle \parallel \gamma$  axis fiber, where  $\gamma$  is the SPN and compression direction. It also has a weaker  $\langle 100 \rangle \parallel \gamma$  fiber. The fibers can be clearly seen in the PFs of Figure 5. A similar weak fiber texture (with even lower intensity) is observed after compaction of another powder sample of the same alloy as well as of the Pd-10Au compacted powder (Figure 5)<sup>[3]</sup> with the  $\langle 100 \rangle$  fiber being absent.

The local texture as a function of shear strain is shown in Figure 4. The maximum ODF intensity and the volume fraction of the  $\langle 110 \rangle$  fiber in radial direction of the disc from the center to the edge, i.e., as a function of shear strain, is shown in Figure 6. The texture varies in radial direction showing that it is quite inhomogeneous within the disc. Despite this variation, the texture seems to further weaken with shear strain. The typical texture components developing in fcc metals during simple shear (Table 2) as observed for nc materials with coarser grain size<sup>[3–8]</sup> can be weakly identified at high shear strains. Otherwise, the intensity of the  $\langle 110 \rangle$  fiber seems to spread toward the shear components (Figure 4). Generally, the  $\langle 110 \rangle$  fiber represents a typical compression texture of fcc metals developing through dislocation glide.<sup>[34]</sup>

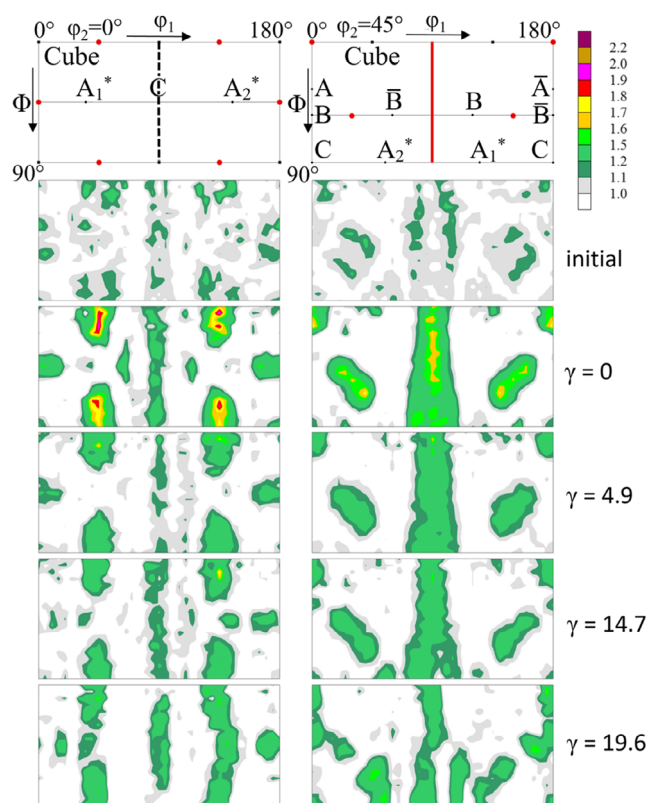


**Figure 4.** Texture represented as  $\phi_2 = 0^\circ$  and  $\phi_2 = 45^\circ$  ODF-sections at different shear strains  $\gamma$  after compaction of igc powder (initial), intensities are given in multiples of a random orientation distribution. The key figure shows the main texture components (for component designation see Table 2) that develop during simple shear of fcc metals. Red dots and red line mark the  $\langle 110 \rangle$  fiber, and black squares (Cube) and black dashed line mark the  $\langle 100 \rangle$  fiber parallel to the SPN.

The results of the texture simulations are shown in Figure 7 for the powder compaction stage after a compression strain of 0.27, and for HPT deformation at three shear strain values. As can be seen, the texture is quite precisely predicted for powder compaction, both in terms of texture components and their intensity. Only the slight  $\langle 100 \rangle$  fiber was not reproduced at sufficient strength. In the case of HPT, the obtained strain partition was increased from 0.31 to 0.37 fraction produced by GBS with respect to the imposed strain (this is the so-called  $R$  ratio in ref. [4]). As can be seen, the simulated texture has the usual components of fcc shear textures (Table 2), with progressive increase of the  $B/\bar{B}$  components, and a weak decreasing  $C$ . However, this predicted HPT deformation texture is very different from the experimental one (Figure 4). This is surprising because the same GBS approach was successfully applied to the Pd-10Au alloy for grain sizes  $> 20 \text{ nm}$ .<sup>[3,4]</sup> The difference in the present case is that the alloy is on the other side of the phase diagram with a slightly higher homologous deformation temperature and a significantly lower SFE, and the saturation grain size is also smaller. The precise reasons for this discrepancy will be elucidated in the discussion part.

To get insight in the role of GBS, a special simulation was carried out, when the deformation was almost exclusively

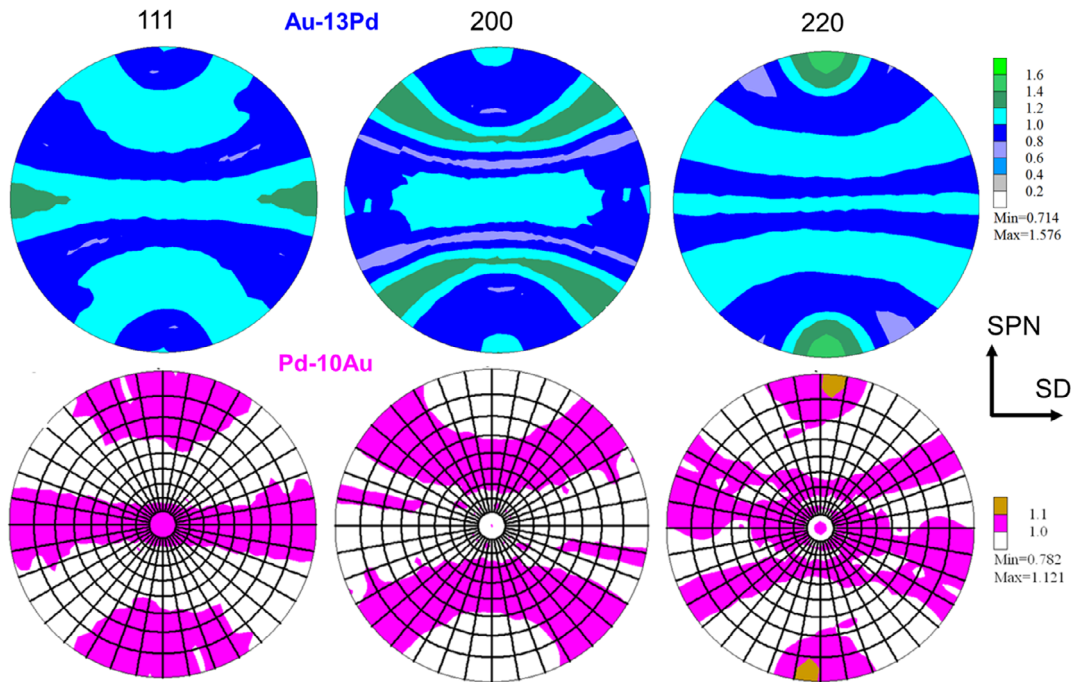


**Figure 5.** Texture at  $\gamma=0$  of Au-13Pd and Pd-10Au alloys represented as PFs 111, 200, and 220 (SPN = shear plane normal = compression axis, SD = shear direction, intensities are given in multiples of a random orientation distribution).

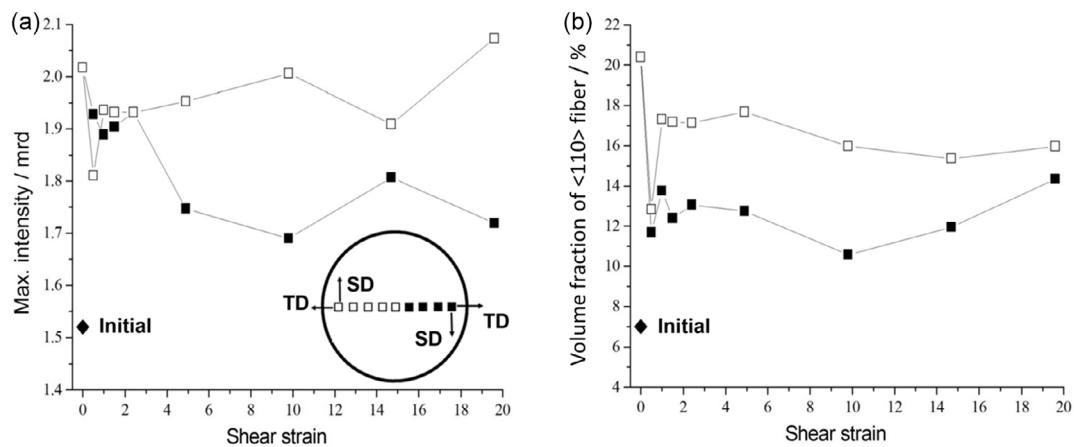


**Figure 6.** a) Maximum ODF intensity and b) volume fraction of <110> fiber (15° spread) as a function of shear strain for Au-13Pd. The inset in (a) shows the measurement path in radial direction from the center to the edge.

produced by GBS. For achieving that, the relative strength of GBS was set extremely low with respect to the  $\{111\}\langle 112 \rangle$  and  $\{111\}\langle 110 \rangle$  slip system families; the ratios were 0.001/1.0/1.5, respectively. The obtained texture is displayed in **Figure 8** for the shear strain value of 4.9. As can be seen, the texture is still composed of the  $B/\bar{B}$  components, with the difference that they are rotated around TD of the sample (represented by the  $\varphi_1$  angle) by about 16°, in the direction of the shear. The texture strength is reduced significantly with respect to the same case in Figure 7; the maximum intensity is decreased from 9.19 to 3.87. These main features of the simulated textures remained about the same

for this extreme high GBS when the strain was further increased (note that the construction of the GBS model does not permit the total elimination of the crystallographic slip systems, so it is not possible to impose 100% GBS).

#### 4. Discussion

It is a general observation that during severe plastic deformation (SPD) after a certain imposed strain depending on the material the microstructure becomes stationary.<sup>[27]</sup> **Table 3** compares the

**Table 2.** Texture components of simple shear deformed fcc metals and their crystallographic description  $\{hkl\}\langle uvw \rangle$  with regard to shear plane and shear direction.

Component designation	Miller indices $\{\text{shear plane}\}\langle \text{shear direction} \rangle$
A	$\{1\bar{1}\bar{1}\}\langle 110 \rangle$
$\bar{A}$	$\{\bar{1}11\}\langle \bar{1}\bar{1}0 \rangle$
$A_1^*$	$\{\bar{1}\bar{1}1\}\langle 112 \rangle$
$A_2^*$	$\{11\bar{1}\}\langle 112 \rangle$
B	$\{\bar{1}12\}\langle 110 \rangle$
$\bar{B}$	$\{1\bar{1}\bar{2}\}\langle \bar{1}\bar{1}0 \rangle$
C	$\{001\}\langle 110 \rangle$

stationary values of the microstructure parameters of HPT-processed Au-13Pd with those measured for nc fcc metal alloys of different SFE, or SFE values normalized with shear modulus  $G$  and Burgers vector  $b$ . It can be seen that the Au-13Pd alloy falls into the general trend: i) The saturation crystallite size of all alloys is almost the same. However, within the Au-Pd alloy system, it is slightly lower for Au-13Pd, although the homologous deformation temperature is higher. The reason could therefore be a lower grain boundary mobility due to the different alloy composition.

Taking into account all alloys in Table 3, it can be seen that the SFE is not the controlling parameter. The initial microstructure of a single-phase material does not affect the saturation grain size.<sup>[42,43]</sup> In general, application of HPT results in grain size refinement of coarser-grained, single-phase materials<sup>[7,27]</sup> and grain coarsening of finer-grained materials, this study and,<sup>[3,21,44]</sup> whereby both processes lead to almost the same saturation grain size.<sup>[42]</sup> For a detailed study and discussion of variations in saturation grain size in relation to physical parameters such as melting temperature, diffusivity, valence electrons, SFE, and solute dislocation interactions, see ref. [45]. ii) The dislocation density and the dislocation arrangement parameter increase with decreasing SFE, while the dislocation character in all cases is almost screw-type. The first two effects are due to a reduced dynamic recovery rate, which depends on the degree of dislocation dissociation hindering both cross slip and climb, thereby retarding dislocation annihilation. The equilibrium width of dissociated dislocations is inversely related to SFE/ $Gb$ . When the initial dislocation density is smaller or bigger than the stationary one, the dislocation density increases during SPD<sup>[7,27]</sup> or decreases, this study and ref. [3]. Gubicza<sup>[27]</sup> related the stationary grain and crystallite size determined by transmission electron microscopy (TEM) and XLP, respectively, to the stationary dislocation density determined by XLP. In a double logarithmic plot, the grain size decreases almost linearly with increasing dislocation density with the power  $-2/3$ , while for the smaller

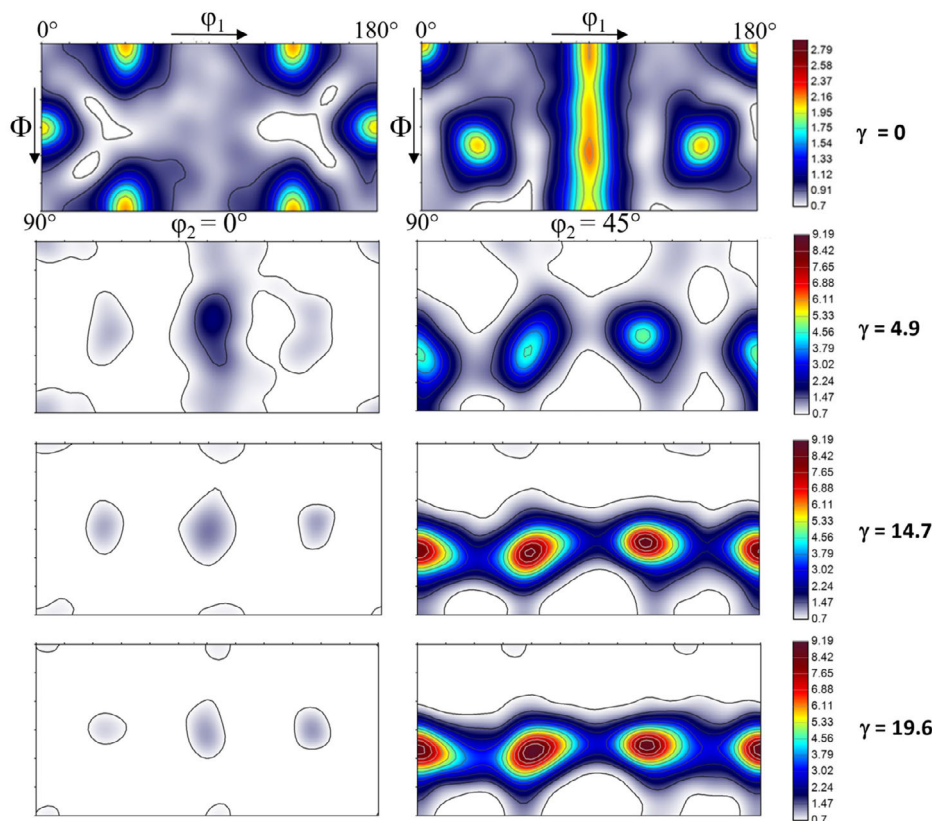


**Figure 7.** Simulated textures are represented as  $\varphi_2 = 0^\circ$  and  $\varphi_2 = 45^\circ$  ODF-sections for the end of the powder compaction stage (at a compression strain of 0.27), indicated by  $\gamma = 0$ , and for HPT testing at increasing shear strains. For the latter, the GBS approach of ref. [4] was used starting with the experimental initial texture at  $\gamma = 0$  in Figure 4. Intensities are given in multiples of a random orientation distribution.

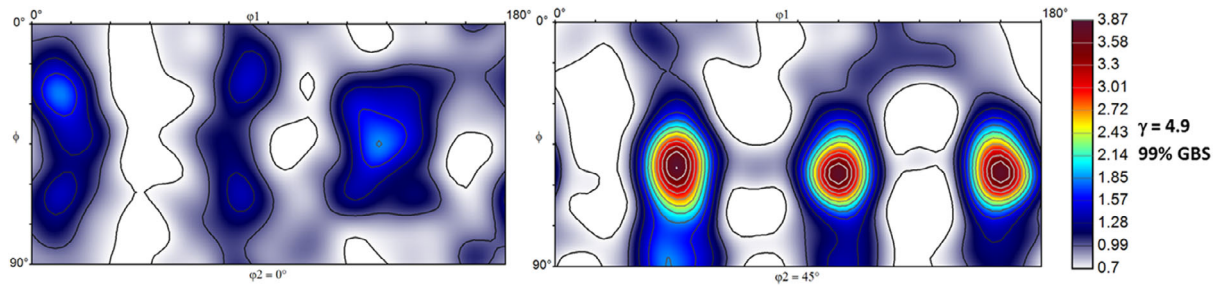


**Figure 8.** Simulated texture for 99% GBS at a shear strain of  $\gamma = 4.9$  (intensities are given in multiples of a random orientation distribution).

**Table 3.** Saturation values of microstructure parameters measured for nc fcc metal alloys of different SFE HPT-processed at RT (igc, inert gas condensation; AM, additively manufactured; G, shear modulus; b, magnitude of the Burgers vector).

	SFE [ $\text{mJ m}^{-2}$ ] ( $10^3$ SFE/Gb)	G [GPa]	B [nm]	$\langle x \rangle_a$ [nm]	$\rho$ [ $10^{16} \text{ m}^{-2}$ ]	$q$	$M$	$\beta_{\text{TW}}$ [%]	$\beta_{\text{SF}}$ [%]
Pd-10Au (igc) <sup>[3]</sup>	150 <sup>[15]</sup> (12.4)	44 <sup>a)</sup>	0.275 <sup>[3]</sup>	24	1.3	2.2 <sup>b)</sup>	0.5 <sup>b)</sup>	–	1
Au-13Pd (igc)	40 <sup>[15]</sup> (4.8)	29 <sup>a)</sup>	0.286	20	2	1.9	0.9	2.5	–
CrMnFeCoNi (cast) <sup>[7]</sup>	30 <sup>[35]</sup> (1.5)	79 <sup>[35]</sup>	0.255 <sup>[35]</sup>	24	3	2.3	5	2 <sup>c)</sup>	–
316L steel (AM) <sup>[36]</sup>	26 <sup>[37]</sup> (1.3)	78 <sup>[38]</sup>	0.254 <sup>[39]</sup>	$\approx 30$	3–3.5			3.5–4	

<sup>a)</sup> Estimated from the values of Pd (46 GPa<sup>[40]</sup>) and Au (27 GPa<sup>[41]</sup>) using the rule of mixtures; <sup>b)</sup> Unpublished; <sup>c)</sup> Maximum value at a shear strain of 25.

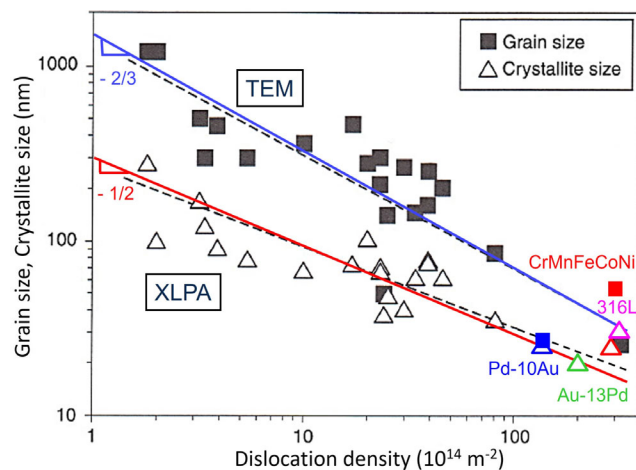


**Figure 9.** Saturation grain and crystallite size determined by TEM and XLPAs, respectively, for metallic materials processed by SPD as a function of saturation dislocation density (according to ref. [27]) expanded by values of nc alloys (in color) listed in Table 3. The slopes of the red and blue lines are  $-1/2$  and  $-2/3$ , respectively.

crystallite size, it is  $-1/2$  (Figure 9). The values of nc alloys listed in Table 3 fit well into these relations. Within the large spread of the data, in the lowest nanorange of about 20 nm, the crystallite size is comparable to the grain size and the dislocation density is about  $4 \times 10^{16} \text{ m}^{-2}$ . Thus, there seems to be a lower limit of grain refinement and a maximum limit of accumulation of dislocation density during SPD. This may be due to the transition from dislocation to grain boundary-mediated plasticity, see the following paragraph. iii) According to XLPAs, the line profiles of Pd-10Au and Au-13Pd were best fitted by assuming stacking

faults (SFs) and deformation twinning, respectively. Thus, a transition from SFs to mechanical twins occurs with decreasing SFE, with the twin density increasing as the SFE decreases. According to ref. [27], all the mechanisms proposed for deformation twinning are based inherently on the dissociation of lattice dislocations into twinning partials and their slip on successive  $\{111\}$  planes. This explains the observed dependence on SFE/Gb.

The texture of the nc Au-13Pd does not change much during HPT. It is characterized by a dominant  $\langle 110 \rangle$  fiber already developed during powder compaction. The intensity of this fiber decreases slightly with shear strain. Only at shear strains above about 15 minor shear components developed. The experimental compaction texture can be simulated by using a GBS approach<sup>[4]</sup> involving nearly free rotations and sliding of the particles as well as fully relaxed deformation components.<sup>[32]</sup> However, in the unrelaxed version, the HPT texture is by no means reproduced, in contrast to former results on Au-10Pd for grain sizes  $> 20 \text{ nm}$ .<sup>[3,4]</sup> It should be emphasized that in Au-10Pd, the compaction texture (Figure 5) also did not change significantly during HPT-induced grain growth to about 20 nm. It can therefore be assumed that the grain size range up to around 20 nm is the reason for the lack of shear texture development in both alloys. Consequently, another GBS mechanism must be in operation, as shown in Figure 10. In this approach of GBS, planar interfaces are produced by grain boundary migration.<sup>[11]</sup> Once a planar interface is formed, the localized sliding shears can result in mesoscopic sliding across the dimensions of many grains and result in large shear strains without work hardening (Figure 1). The advantage of this approach is that grain boundary migration is more effective in reducing steric hindrance than diffusion. Diffusion distances are only in the order of magnitude of the grain boundary width  $\delta$ . As the grain size of the material

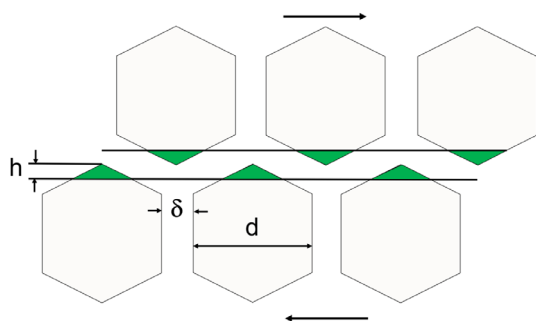


**Figure 10.** GBS mechanism of nanomaterials with grain size  $d$  and grain boundary width  $\delta$  for  $\delta/d \geq 0.025$ . The layer of thickness  $h$  represents a mesoscopic planar interface produced by grain boundary migration by replacing the atoms located in the green regions (according to ref. [11]).

decreases (or the ratio of  $\delta$  to grain size  $d$  increases), the steric hindrance tends to decrease. As can be seen in Figure 10, the amount of material, corresponding to the number of atoms (proportional to the dimension  $h$ ), that must be displaced to form a mesoscopic planar interface is a fraction of the grain size and becomes comparable to the grain boundary width for the lowest range of the nc regime. For  $\delta = 0.5 \text{ nm}^{[46]}$  and  $d \leq 20 \text{ nm}$ ,  $\delta/d \geq 0.025$ . According to this GBS approach, the initial texture should not change during shearing. Such planar interfaces expanding over several grains were experimentally observed in HPT-processed Pd.<sup>[21]</sup>

Finally, the strength difference between the two Au-Pd alloys (Figure 1) is discussed based on the parameters listed in Table 3. HPT of Au-13Pd requires lower torque/shear stress than HPT of Pd-10Au, in qualitative agreement with yield stress and microhardness measurements on as-IGC material (initial, less dense state).<sup>[40]</sup> For both alloys below about 20 nm, the GBS mechanism explained above dominates. While this applies to Au-13Pd for the entire shear strain range, for Pd-10Au, because of deformation-induced grain growth after a certain shear strain, there is a shift to sliding of partial/full dislocations emitted from grain boundaries.<sup>[3]</sup> The change in the deformation mechanism may be responsible for the higher strength and work hardening of Pd-10Au. In contrast, both deformation mechanisms scale with the shear modulus, which is about 50% higher for Pd-10Au than for Au-13Pd (Table 3). Other reasons for the strength difference can also be grain boundary segregation and/or deformation-induced structural relaxation of the grain boundaries.<sup>[47,48]</sup> However, using a combination of Monte Carlo and molecular dynamics methods, Schäfer et al.<sup>[15]</sup> for Pd/Au concentrations up to about 10% showed that the equilibrium solute configuration in the grain boundaries is not different from that of the random solid solution found in the bulk. Experimental proof of this prediction is still awaited. Deformation-induced (and thermally-induced) structural relaxation of the grain boundaries leads to a lowering of the grain boundary energy and thus stability of the nc structure and an increase in strength.<sup>[49]</sup> It is assumed that grain boundary relaxation is induced by the emission of partial dislocations or twins from grain boundaries. Therefore, according to Table 3, the effect must be favored by SFs.

## 5. Conclusion

In the Au-Pd alloy system, the nc structure of Au-13Pd was found more stable than that of Pd-10Au on the other side of the phase diagram during HPT at room temperature. This may be due to the different alloy composition. Furthermore, the compaction texture of the igc powder did not change during SPD. Based on the texture simulations employed, it is concluded that with decreasing grain size at around 20 nm, a transition in GBS mechanism takes place from grain-scale GBS to mesoscopic cooperative GBS on planar interfaces produced by grain boundary migration. Once a planar interface is formed, the localized sliding shears can result in mesoscopic sliding across the dimensions of many grains leading to large shear strains. This GBS mechanism preserves the initial texture.

## Acknowledgements

The nanocrystalline igc Au-13Pd initial material was kindly produced and chemically analyzed by the group of Prof. R. Birringer (FR 7.2 Experimentalphysik, Universität des Saarlandes). LST acknowledges the support from the National Research, Development and Innovation Office, Hungary, under the K143800 project “New avenues of production of bulk and composite nanostructured metals: experiments, characterization, modelling.”

Open Access funding enabled and organized by Projekt DEAL.

## Conflict of Interest

The authors declare no conflict of interest.

## Data Availability Statement

The data that support the findings of this study are available on request from the corresponding author. The data are not publicly available due to privacy or ethical restrictions.

## Keywords

grain boundary sliding, high-pressure torsion, microstructure, nanocrystalline Au-13Pd alloy, polycrystal modeling, texture

Received: January 26, 2024

Revised: May 15, 2024

Published online: June 7, 2024

- [1] Yu. Ivanisenko, W. Skrotzki, R. Chulist, T. Lippmann, L. Kurmanaeva, H.-J. Fecht, *J. Mater. Sci.* **2010**, *45*, 4571.
- [2] Yu. Ivanisenko, W. Skrotzki, R. Chulist, T. Lippmann, L. Kurmanaeva, *Scr. Mater.* **2012**, *66*, 131.
- [3] W. Skrotzki, A. Eschke, B. Jóni, T. Ungár, L. S. Tóth, *Acta Mater.* **2013**, *61*, 7271.
- [4] Y. Zhao, L. S. Toth, R. Massion, W. Skrotzki, *Adv. Eng. Mater.* **2017**, *20*, 1700212.
- [5] L. S. Toth, W. Skrotzki, Y. Zhao, A. Pukenas, C. Braun, R. Birringer, *Materials* **2018**, *11*, 190.
- [6] W. Skrotzki, A. Pukenas, B. Jóni, E. Odor, T. Ungár, A. Hohenwarter, R. Pippan, *IOP Conf. Ser. Mater. Sci. Eng.* **2017**, *194*, 012028.

- [7] W. Skrotzki, A. Pukenas, E. Odor, B. Jóni, T. Ungár, B. Völker, A. Hohenwarter, R. Pippin, *Crystals* **2020**, *10*, 336.
- [8] S. N. Kumaran, S. K. Sahoo, C. Haase, L. A. Barrales-Mora, L. S. Tóth, *Acta Mater.* **2023**, *250*, 118814.
- [9] A. Chokshi, A. Rosen, J. Karch, H. Gleiter, *Scr. Metall.* **1989**, *23*, 1679.
- [10] S. N. Naik, S. Walle, *J. Mater. Sci.* **2020**, *55*, 2661.
- [11] H. Hahn, P. Mondal, K. A. Padmanabhan, *Nanostruct. Mater.* **1997**, *9*, 603.
- [12] M. Grever, C. Braun, M. J. Deckarm, J. Lohmiller, P. A. Gruber, V. Honkimäki, R. Birringer, *Mech. Mater.* **2017**, *114*, 254.
- [13] L. Li, T. Ungár, L. S. Toth, W. Skrotzki, Y. D. Wang, Y. Ren, H. Choo, Z. Fogarassy, X. T. Zhou, P. K. Liaw, *Metall. Mater. Trans. A* **2016**, *47*, 6632.
- [14] H. Okamoto, T. B. Massalski, *Bull. Alloy Phase Diagrams* **1985**, *6*, 229.
- [15] J. Schäfer, A. Stukowski, K. Albe, *Acta Mater.* **2011**, *59*, 2957.
- [16] H. Gleiter, *Prog. Mater. Sci.* **1989**, *33*, 233.
- [17] M. Ames, J. Markmann, R. Karos, A. Michels, A. Tschöpe, R. Birringer, *Acta Mater.* **2008**, *56*, 4255.
- [18] R. Pippin, S. Scheriau, A. Hohenwarter, M. Hafok, *Mater. Sci. Forum* **2008**, *584–586*, 16.
- [19] A. Nadai, in *Theory of Flow and Fracture of Solids*, 2nd ed., Mc Graw-Hill, New York, NY **1950**.
- [20] A. Pougis, S. Philippon, R. Massion, L. Faure, J.-J. Fundenberger, L. S. Toth, *Tribology Int.* **2013**, *67*, 27.
- [21] Yu. Ivanisenko, L. Kurmanaeva, J. Weissmüller, K. Yang, J. Markmann, H. Rösner, T. Scherer, H.-J. Fecht, *Acta Mater.* **2009**, *57*, 3391.
- [22] D. V. Bachurin, P. Gumbsch, *Modell. Simul. Mater. Sci. Eng.* **2014**, *22*, 025011.
- [23] J. Gubicza, in *X-Ray Line Profile Analysis in Materials Science*, IGI-Global, Hershey, PA **2014**.
- [24] T. Ungar, S. Ott, P. G. Sanders, A. Borbely, J. R. Weertman, *Acta Mater.* **1998**, *46*, 3693.
- [25] L. Balogh, G. Ribarik, T. Ungar, *J. Appl. Phys.* **2006**, *100*, 023512.
- [26] G. Ribarik, B. Jóni, T. Ungar, *J. Mater. Sci. Technol.* **2019**, *35*, 1508.
- [27] J. Gubicza, in *Defect Structure in Nanomaterials*, Woodhead Publishing, Cambridge **2012**.
- [28] *Multex Manual, Multex 3*, Bruker AXS GmbH, Karlsruhe **2008**.
- [29] K. Pawlik, *Phys. Stat. Sol. B* **1986**, *134*, 477.
- [30] H.-J. Bunge, *Z. Metallkde* **1965**, *56*, 872.
- [31] L. S. Tóth, A. Molinari, *Acta Metall. Mater.* **1994**, *42*, 2459.
- [32] L. S. Toth, W. Skrotzki, A. Pukenas, Yu. Ivanisenko, N. Yazbek, to be published.
- [33] B. Beausir, J.-J. Fundenberger, *Analysis Tools For Electron and X-ray Diffraction*, ATEX - Software, www.atex-software.eu, Université de Lorraine, Metz **2017**.
- [34] A. D. Rollett, S. I. Wright, in: *Texture and Anisotropy*, Cambridge University Press, Cambridge **1998**, p. 179.
- [35] N. L. Okamoto, S. Fujimoto, Y. Kambara, M. Kawamura, Z. M. Chen, H. Matsunishi, K. Tanaka, H. Inui, E. P. George, *Sci. Rep.* **2016**, *6*, 35836.
- [36] J. Gubicza, M. Kawasaki, Z. Dankházi, M. Windisch, M. El-Tahawy, *J. Mater. Sci.* **2024**, *59*, 6008.
- [37] G. M. de Bellefon, J. C. van Duysen, K. Sridharan, *J. Nucl. Mater.* **2017**, *492*, 227.
- [38] Y. M. Wang, T. Voisin, J. T. McKeown, J. Ye, N. P. Calta, Z. Li, Z. Zeng, Y. Zhang, W. Chen, T. T. Roehling, R. T. Ott, M. K. Santala, P. J. Depond, M. J. Matthews, A. V. Hamza, T. Zhu, *Nat. Mater.* **2018**, *17*, 63.
- [39] D. Molnár, X. Sun, S. Lu, W. Li, G. Engberg, L. Vitos, *Mater. Sci. Eng. A* **2019**, *759*, 490.
- [40] M. Grever, *PhD Thesis*, Universität des Saarlandes **2013**.
- [41] <https://material-properties.org/gold-mechanical-properties-strength-hardness-crystal-structure>.
- [42] R. Pippin, S. Scheriau, A. Taylor, M. Hafok, A. Hohenwarter, A. Bachmaier, *Annu. Rev. Mater. Res.* **2010**, *40*, 319.
- [43] O. Renk, R. Pippin, *Mater. Trans.* **2019**, *60*, 1270.
- [44] X. Z. Liao, A. R. Kilmametov, R. Z. Valiev, H. Gao, X. Li, A. K. Mukherjee, J. F. Bingert, Y. T. Zhu, *Appl. Phys. Lett.* **2006**, *88*, 021909.
- [45] K. Edalati, D. Akama, A. Nishio, S. Lee, Y. Yonenaga, J. M. Cubero-Sesin, Z. Horita, *Acta Mater.* **2014**, *69*, 68.
- [46] D. Prokoshkina, V. A. Esin, G. Wilde, S. V. Divinski, *Acta Mater.* **2013**, *61*, 5188.
- [47] C. A. Schuh, K. Lu, *MRS Bull.* **2021**, *46*, 225.
- [48] Y. A. Sun, Z. P. Luo, X. Y. Li, K. Lu, *Acta Mater.* **2022**, *239*, 118256.
- [49] J. Hu, Y. N. Shi, X. Sauvage, G. Sha, K. Lu, *Science* **2017**, *355*, 1292.